Materials Advances

ROYAL SOCIETY OF CHEMISTRY

PAPER

View Article Online
View Journal | View Issue

Cite this: *Mater. Adv.*, 2024, 5, 2169

Efficient photocatalytic chloride dehalogenation by planar conjugated microporous polymers with enhanced charge separation and transport†‡

Hao Zhang,[a] Sizhe Li,[a] Zhuangfei Qian,[a] Jie Yin,[a] Wenxin Wei,*[a] Yan Zhao*[ab] and Kai A I Zhang[a]

Received 12th November 2023,
Accepted 19th January 2024

DOI: 10.1039/d3ma00994g

rsc.li/materials-advances

Conjugated microporous polymers (CMPs) exhibiting semiconductor properties have been widely employed as heterogeneous photocatalysts. Photogenerated charge carrier separation and transfer are crucial factors influencing the performance of such photocatalysts. Typically, the electron/acceptor units linked by carbon–carbon single bonds tend to form larger dihedral angles due to steric hindrance, thus inhibiting the transport of charge carriers, leading to recombination of photogenerated electro-hole pairs and consequently limiting the photocatalytic performance of the material. Based on this, we designed two CMPs, one with a planar structure, dibenzo[*g*,*p*]chrysene (DBC), and the other with a non-planar structure, tetraphenylethylene (TPE), to investigate the influence of planarity on the catalytic performance of the materials. Theoretical simulation results reveal that CMP-DBC, with its planar structure, has a significantly smaller dihedral angle for the electron donor (18.4°) compared to CMP-TPE (47.8°). According to calculations from temperature-dependent fluorescence spectroscopy, the exciton binding energy of the former (108 meV) is also smaller than that of the latter (126 meV). In the photocatalytic dehalogenation reaction, CMP-DBC achieves nearly 100% halide product yield, far surpassing the 60% yield of CMP-TPE. Both theoretical and experimental results indicate that CMP-DBC, with its smaller donor–acceptor dihedral angle, facilitates charge carrier migration, effectively suppressing rapid radiative recombination, and thus exhibits superior photocatalytic performance.

1. Introduction

The global population growth, urbanization, and increasing agricultural production have placed growing pressures on nature. In particular, the use of chemicals in agriculture, industry, and pharmaceuticals has introduced new challenges for the environment.[1–3] Halogenated organic compounds have gained increasing attention due to their threats to aquatic life and human health. These compounds are persistent pollutants that often elude conventional wastewater treatment methods, resulting in their accumulation in the environment and posing serious threats to ecosystem health.[4–7] These organic compounds find wide applications in various industries and consumer products, including pesticides, flame retardants, disinfectants, insecticides, dyes, dielectrics, coolants, plant growth regulators, plasticizers, and pharmaceuticals.[8–11] Their high toxicity, persistence, bioaccumulation potential, and widespread distribution have led to severe environmental pollution.[12] In this context, effective methods for the degradation of these halogenated organic pollutants are required. Over the past few decades, extensive efforts have been made in the degradation of halogenated organic pollutants (HOPs). Notably, several processes have been developed to break the strong C–X bonds (X = F, Cl, Br, and I) present in HOPs. These processes include microbial degradation,[13,14] ionizing radiation,[15,16] metal reduction,[17–19] electrocatalysis,[20–22] sonolysis,[23] and photocatalysis.[24,25] Photocatalysis stands out due to its ease of implementation, high efficiency, safety, and environmental compatibility.[26–28]

Photocatalysis has recently garnered increased attention, emerging as a potent method for the degradation of halogenated aromatic pollutants.[28–30] During exposure to light, photogenerated species directly participate in the reduction and dehalogenation or transform into secondary catalytic active substances. Photocatalysts encompass classical molecular photosensitizers[31,32] and semiconductor materials (metal oxides,[33,34] metal sulfides,[35–37] and organic frameworks,[38–41] among others). Among these materials, conjugated microporous polymers (CMPs) have emerged as promising candidates due to their tunable porous structures and photoactive

[a] *Department of Materials Science, Fudan University, Shanghai 200438, P. R. China. E-mail: weiwenxin@fudan.edu.cn, zhaoy@fudan.edu.cn*
[b] *State Key Laboratory of Luminescent Materials and Devices, South China University of Technology, Guangzhou 510640, China*

† We would like to dedicate this paper to the memory of Prof. Kai Zhang, who unfortunately passed away just as the manuscript was nearing completion. Kai played an essential role in the research described here and he is truly missed.

‡ Electronic supplementary information (ESI) available. See DOI: https://doi.org/10.1039/d3ma00994g

properties. However, in the process of developing highly efficient photocatalysts based on CMPs, a long-standing challenge has been the internal dihedral angles between electron donor and acceptor units within the polymer structure. This angle often restricts charge separation and transport, consequently affecting the overall photocatalytic performance.[42–45] To overcome this limitation and promote the effective separation and migration of photogenerated charge carriers, novel design strategies addressing the molecular arrangement of polymer components are urgently needed.

Herein, we focused on the synthesis and application of planar conjugated microporous polymers (CMP-DBC) with dibenzo[*g*,*p*]chrysene (DBC) as the planar structural unit. The inherent planarity of dibenzo[*g*,*p*]chrysene holds the potential to enhance charge separation and transport by minimizing internal dihedral angles (Scheme 1). Furthermore, benzothiadiazole (BT) serves as a strong electron donor and acceptor, effectively promoting photoinduced charge transfer processes. To elucidate the significance of this design, we conducted a comparative analysis with the non-planar CMP counterpart, CMP-TPE. While structurally similar to DBC, TPE's non-planarity provides a basis for evaluating the impact of molecular planarity on CMP photocatalytic performance. Through the utilization of various characterization techniques, including temperature-dependent fluorescence measurement, photocurrent analysis, and electrochemical impedance spectroscopy (EIS), we established that CMP-DBC exhibits superior charge separation and migration compared to CMP-TPE. The enhanced charge dynamics within CMP-DBC is expected to be reflected in its photocatalytic efficiency. Furthermore, our research delved into the photocatalytic reductive dehalogenation of organic chlorides as a model reaction. Particularly noteworthy is the significant enhancement in dehalogenation efficiency of CMP-DBC under visible light, emphasizing the practicality of this approach.

2. Experimental procedure

The synthesis and characterization of CMP-DBC and CMP-TPE are provided in the ESI.‡

3. Results and discussion

We can observe a significant difference in the intramolecular rotation between the tetraphenylethylene (TPE) building block (θ = 47.8°) and dibenzo[*g*,*p*]chrysene (DCB) (θ = 18.4°). This difference leads to a much lower degree of conformational freedom in DCB and results in less intramolecular rotation-induced energy dissipation. The structure of CMP-DBC, constructed with DCB as a planar strong electron donor and benzothiadiazole as an electron acceptor, is depicted in Fig. 1. In contrast, CMP-TPE was synthesized with tetraphenylethylene (TPE) as the electron donor, which possesses a similar but non-planar structure to DCB. Characterization of the morphology of both CMPs was conducted using scanning electron microscopy (SEM) and transmission electron microscopy (TEM). These analyses revealed that both CMPs exhibited a fused particle-type morphology similar to the previously reported CMP. Solid-state cross-polarization ^{13}C NMR spectra of both CMPs confirmed the successful presence of the benzothiadiazole unit, as indicated by the characteristic signal peak of the sp^2-hybridized carbon atom at 155 ppm. Notably, the ^{13}C NMR of CMP-TPE exhibited an additional characteristic peak at 140–150 ppm compared to CMP-DBC. This extra peak

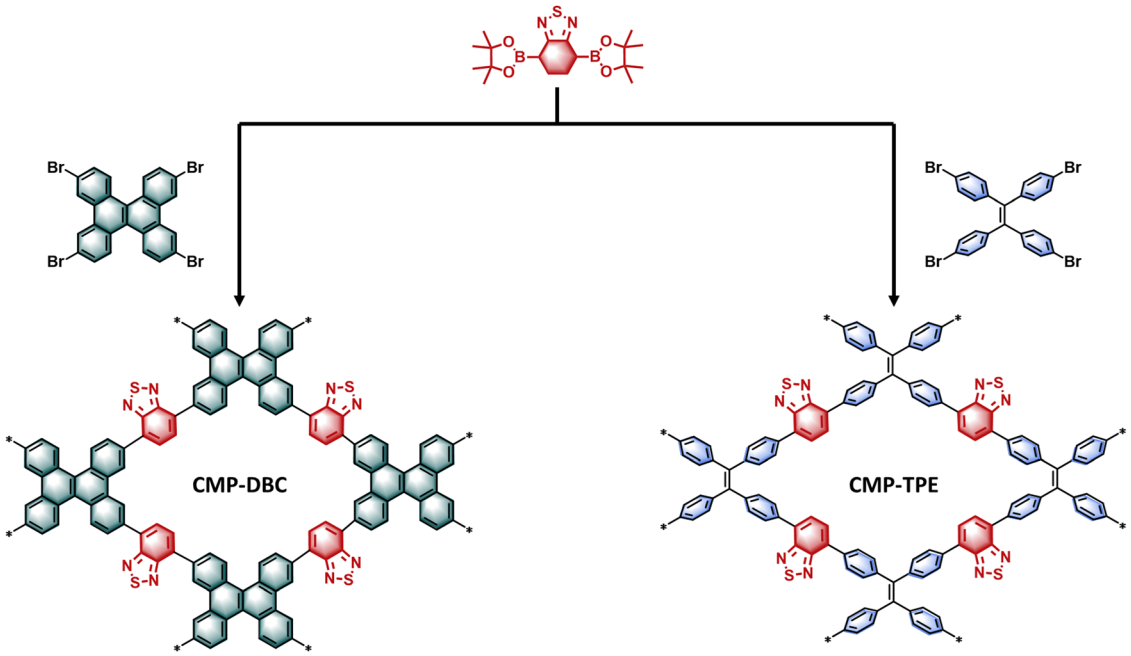

Scheme 1 The synthetic routes for the two polymers and the notional structures.

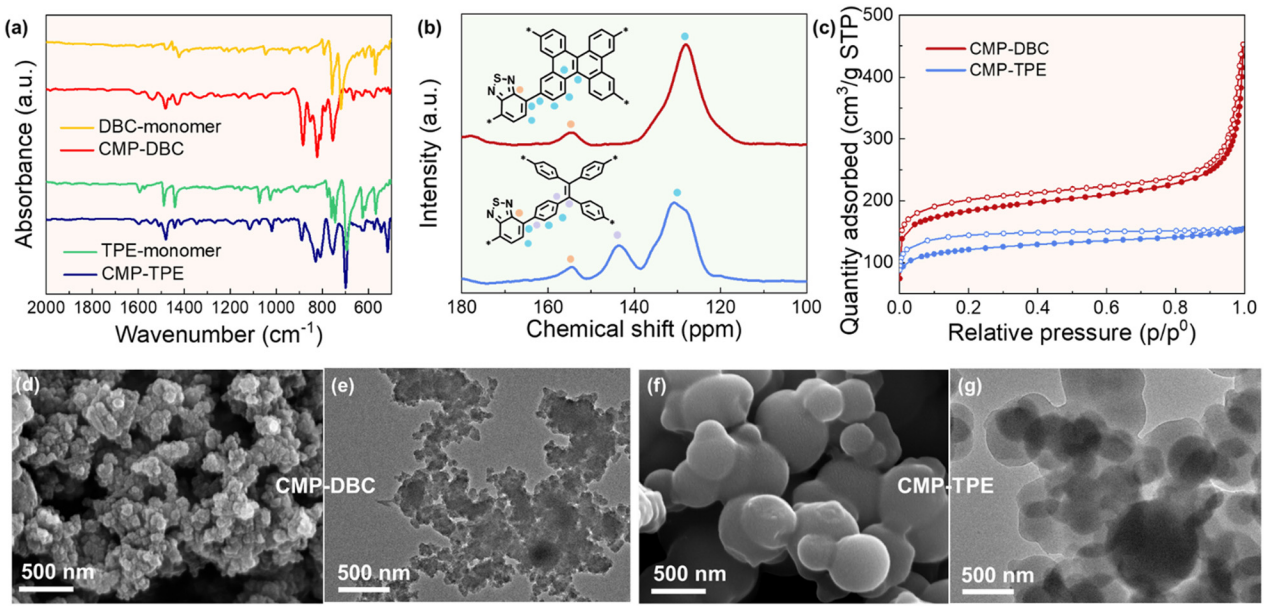

Fig. 1 The structural characterizations of CMP-DBC and CMP-TPE. (a) FT-IR spectra; (b) solid-state ^{13}C NMR spectra and the assignment of the carbon atoms in the polymers; (c) nitrogen sorption isotherms; (d) and (e) SEM and TEM images of CMP-DBC; (f) and (g) SEM and TEM images of CMP-TPE.

was caused by the free rotation of the benzene ring in TPE, leading to a weakened conjugation of vinyl. According to the Fourier transform infrared (FT-IR) spectra of the monomers and CMPs, the characteristic peak of CMP-DBC at 1440 and 780 cm^{-1} was assigned to the DBC unit, and the characteristic peak of CMP-TPE at 1450, 780, and 700 cm^{-1} was assigned to the TPE unit. Furthermore, the FT-IR spectra of CMP-DBC and CMP-TPE displayed characteristic stretching vibration bands of C═N in the BT unit at 1484 cm^{-1}, further confirming the successful synthesis of the polymers. To assess porosity, N_2 adsorption–desorption measurements at 77 K were conducted. The N_2 adsorption–desorption isotherms demonstrated Type I behavior for both CMP-DBC and CMP-TPE, indicating the presence of micropores in both materials. The calculated Brunauer–Emmett–Teller (BET) surface areas revealed that both CMPs possess a high surface area (684 $m^2\ g^{-1}$ for CMP-DBC and 456 $m^2\ g^{-1}$ for CMP-TPE, respectively). Additionally, pore size distribution analysis based on density functional theory demonstrated a microporous structure with average pore diameters of approximately 1.21 nm for CMP-DBC and 1.6 nm for CMP-TPE (Fig. S1, ESI‡). Additionally, pore size distribution analysis based on density functional theory demonstrated a microporous structure with average pore diameters of approximately 1.21 nm for CMP-DBC and 1.36 nm for CMP-TPE. The thermogravimetric analysis

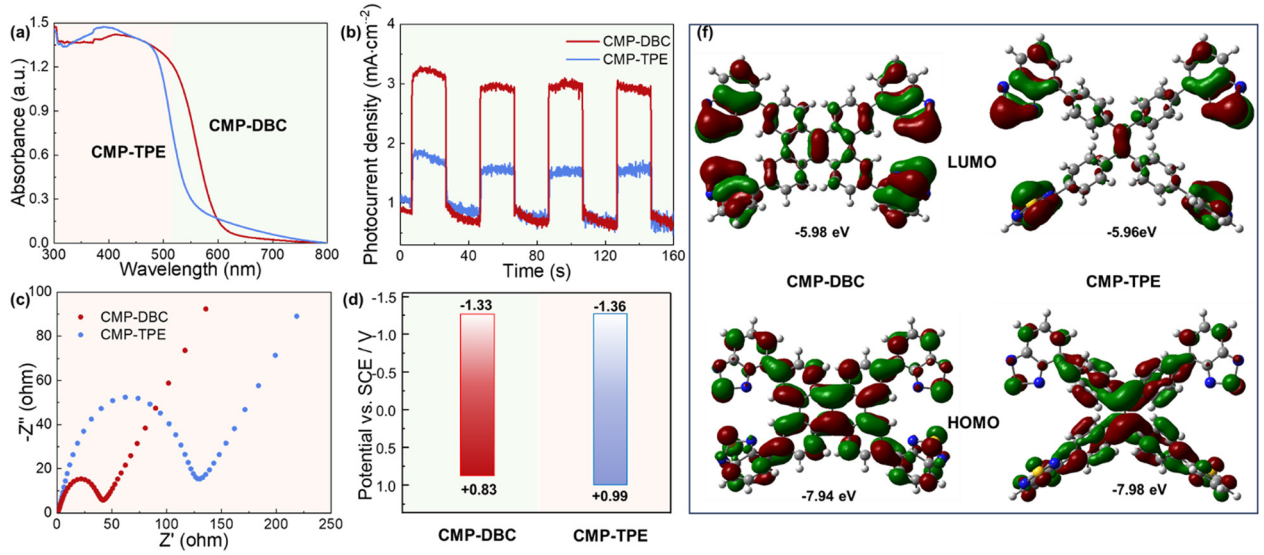

Fig. 2 Photophysical properties of the two polymers. (a) UV-Vis reflectance spectra; (b) photocurrent curves; (c) PL spectra; (d) energy band positions; (f) the HOMO and LUMO distribution of the two polymers based on DFT simulation.

revealed that both CMP-DBC and CMP-TPE exhibit high thermal stability of more than 400 °C under a N_2 atmosphere (Fig. S2, ESI‡).

The light absorption ability of both CMPs was characterized using UV-Vis diffuse reflection spectra. Notably, both CMPs exhibited a broad absorption range, which can be attributed to the strongly polarized electric-field resulting from the copolymerization of the strong electron acceptor BT unit and the electron donor polycyclic aromatic hydrocarbon (Fig. 2). Furthermore, the absorption band of CMP-DBC experienced a redshift and extended to 600 nm in comparison to CMP-TPE. This redshift can be attributed to the extended π-conjugation caused by the improved planar structure of the DBC molecule. Consequently, employing the Kubelka–Munk function (Fig. S2, ESI‡), the optical bandgaps were calculated to be 2.16 eV for CMP-DBC and 2.35 eV for CMP-TPE, respectively. To locate the lowest unoccupied molecular orbital (LUMO) levels, cyclic voltammetry measurements were performed on the CMPs. As depicted in Fig. S3 (ESI‡), the CMPs exhibited similar LUMO potentials. However, it's important to note that the highest occupied molecular orbital (HOMO) levels were found to be +0.84 V for CMP-DBC and +1.04 V for CMP-TPE.

To further explore the impact of geometry on the photogenerated charge separation and transport of the CMPs, we conducted photophysical measurements. Notably, we observed a shift in the maximum fluorescence emission wavelength of CMP-DBC towards longer wavelengths when compared with CMP-TPE. Additionally, CMP-DBC exhibited a significantly lower photoluminescence (PL) intensity than CMP-TPE, primarily due to reduced radiative recombination of photogenerated electron–hole pairs. Moreover, the enhanced charge separation and transfer efficiency were corroborated through time-resolved photoluminescence (TRPL) measurements at an excitation wavelength of 400 nm. As illustrated in Fig. 3, the longer average lifetime of CMP-DBC (4.19 ns) indicated extended charge carrier diffusion time. This can be attributed to the more facile separation and transport of photogenerated carriers from the electron donor to the electron acceptor.

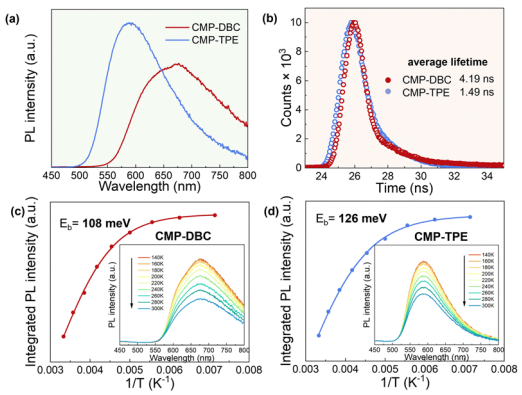

Fig. 3 Photophysical characterization of the two polymers. (a) Photoluminescence spectra; (b) time-resolved photoluminescence spectra; (c) and (d) temperature-dependent fluorescence spectra and activation energy fitting calculation results of CMP-DBC and CMP-TPE.

The kinetic process of photogenerated electron–hole pair separation and transport was elucidated using temperature-dependent fluorescence measurements. Interestingly, both CMPs exhibited a thermal quenching phenomenon, with the PL intensity decreasing as the temperature increased within the range of 140 to 300 K. However, CMP-DBC consistently displayed a notably lower PL intensity than CMP-TPE. By fitting the integrated PL intensities with the Arrhenius equation:

$$I(T) = I_0 \Big/ A\mathrm{e}^{\left(-\frac{E_a}{k_B T}\right)}$$

we obtained the activation energy (E_a) of the PL quenching process. The activation energy for CMP-DBC was estimated to be 108 meV, while that for CMP-TPE was 126 meV. This lower E_a value suggests that non-radiative pathways, such as charge separation, are more favorable in CMP-DBC due to its improved planar structure.

We conducted an investigation into the photoreductive dehalogenation of α-chloroacetophenones as a model reaction, utilizing LED lamp irradiation at 460 nm. Our choice of substrate was α-chloroacetophenones, and we performed condition optimization with diisopropylethylamine (DIPEA) serving as the sacrificial electron donor. As shown in Table 1, using standard reaction conditions in pure water, CMP-DBC achieved nearly complete conversion within just 3 hours, even with a low catalyst load of 5 mg. This performance surpasses that of CMP-TPE, which achieved only a 60% conversion under the same conditions (entries 1 and 2). To emphasize the importance of light and the photocatalyst, we conducted control experiments in darkness, in the presence of oxygen, and without using CMP-DBC as a photocatalyst. These experiments resulted in only trace conversions (entries 3 and 4), clearly demonstrating the indispensable roles of light and the photocatalyst. From entry 5, the presence of oxygen does not impede reactant conversion; however, it drastically reduces the reaction selectivity. We also explored different solvents (entries 6–10). Protonic solvents like methanol and ethanol were found to be less favorable for the reaction conversion. In contrast, when using dichloromethane (CH_2Cl_2) or chloroform ($CHCl_3$) as reaction media, the formation of free radicals led to lower selectivity for acetophenone. Remarkably, conducting the photoreductive dehalogenation reaction in aprotic solvents such as acetonitrile (CH_3CN) and tetrahydrofuran (THF) exhibited excellent catalytic activity and selectivity. The Pd content has no significant influence on the photocatalytic activity. CMP-DBC exhibits higher photocatalytic activity compared to CMP-TPE, despite having a lower Pd residue of 0.463 ppm, suggesting that the Pd residue is not the primary determinant of their disparate photocatalytic activities (Table S1, ESI‡). Therefore, the significant difference in photocatalytic activity between CMP-DBC and CMP-TPE likely originates from variations in electron donor geometries.

To gain a deeper mechanistic understanding of the photoreductive dehalogenation reaction, we conducted a series of experiments to block potential photogenerated active species,

Table 1 Screening and control experiment of the dehalogenation of chlorides

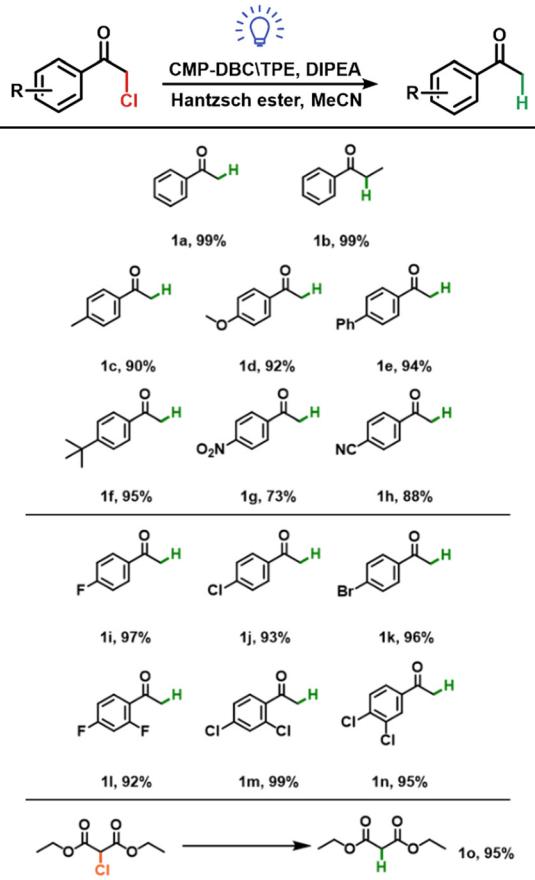

Entry	Catalyst	Solvent	Reaction condition variation	Conversion (%)
1	CMP-DBC	MeCN		99
2	CMP-TPE	MeCN		80
3	CMP-DBC	MeCN	In dark	Trace
4	—	MeCN	No catalyst	Trace
5	CMP-DBC	MeCN	O_2	60
6	CMP-DBC	DMF		67
7	CMP-DBC	DMSO		79
8	CMP-DBC	THF		90
9	CMP-DBC	$CHCl_3$		51
10	CMP-DBC	MeOH		95
11	CMP-DBC	MeCN	No Hantzsch ester	21
12	CMP-DBC	MeCN	No DIPEA	38
13	CMP-DBC	MeCN	Electron scavenger	Trace
14	CMP-DBC	MeCN	Hole scavenger	Trace
15	CMP-DBC	MeCN	Radical scavenger	Trace

focusing on CMP-DBC as the photocatalyst. Notably, we observed reduced yields (<40%) when either the Hantzsch ester or DIPEA was absent (entries 11 and 12). Additionally, the use of $CuCl_2$ as a photogenerated electron scavenger results in trace conversion, highlighting the important role of electrons. Similarly, the conversion of reactants is inhibited when KI is used as a hole scavenger (entry 14). Interestingly, the addition of 2,2,6,6-tetramethylpiperidine-1-oxyl (TEMPO) to trap radicals resulted in only trace amounts of acetophenone, clearly indicating the involvement of radicals in this photoreductive process (entry 15).

We investigated the substrate scope of CMP-DBC under the optimal reaction conditions. As depicted in Table 1, we explored a range of substituted α-chloroacetophenones and α-bromoacetophenones with both electron-donating and electron-withdrawing substituents. Our observations revealed high conversions to the corresponding products in the presence of CMP-DBC, underscoring the broad applicability of CMP-DBC as an efficient photocatalyst. Furthermore, we assessed the stability and reusability of CMP-DBC by conducting repeated experiments. Encouragingly, we observed no significant decrease in catalytic efficiency even after at least five repeated cycles (Fig. S5, ESI‡). Our analysis of the FT-IR spectra (Fig. S6, ESI‡) and UV-Vis spectra (Fig. S7, ESI‡) of CMP-DBC showed minimal changes before and after the repeated reaction.

Building upon the results of the control experiments, we proposed a plausible reaction mechanism. As illustrated in Fig. S8 (ESI‡), we present a relatively straightforward reaction pathway for the reductive transformation of α-chloroacetophenone, which aligns with previous literature. Under visible-light irradiation, α-bromoacetophenone captures an electron from the LUMO level of CMP-DBC, forming intermediate α-carbonyl radicals and chloride anions through a single-electron transfer (SET) process. Subsequently, the sacrificial hydrogen donor (Hantzsch ester) supplies a proton and an electron to the alkyl radical, generating acetophenone. Simultaneously, the deprotonation aromatization of Hantzsch pyridine occurs, facilitated by the use of DIPEA as a deacid agent.

4. Conclusions

In summary, a simple molecular design to facilitate the charge separation and transport within conjugated microporous polymer-based photocatalysts is presented. Through the utilization of various characterization techniques, including temperature-dependent fluorescence measurements, photocurrent analysis and DFT calculation, we have identified that CMP-DBC with a planar geometry structure shows extended π-conjugation, which is conducive to the charge transfer along the polymer chains and leads to the efficient separation of light-induced charge carriers compared to CMP-TPE. As a result, a high conversion above 99% of dehalogenation was successfully achieved by the CMP-DBC photocatalyst under visible light. We believe that this work not only reveals the significant influence of structural design on the photocatalytic activity, but also paves the way for continued exploration of planar conjugated microporous polymers and their role in photocatalysis.

Conflicts of interest

There are no conflicts to declare.

Acknowledgements

The authors acknowledge the National Natural Science Foundation of China (Grants No. 52173198 and 52303267), the China Postdoctoral Science Foundation (Certificate No. 2023M730615)

and the State Key Laboratory of Luminescent Materials and Devices Research Project (2022-skllmd-16) for financial support.

Notes and references

1 I. Twardowska, S. Stefaniak, H. E. Allen and M. M. Häggblom, *Soil and water pollution monitoring, protection and remediation*, Springer Science & Business Media, 2007.
2 M. J. Krzmarzick and P. J. Novak, *Appl. Microbiol. Biotechnol.*, 2014, **98**, 6233–6242.
3 R. Xu, Y. Xie, J. Tian and L. Chen, *J. Cleaner Prod.*, 2021, **283**, 124645.
4 N. Sheik Abdul and J. L. Marnewick, *J. Appl. Toxicol.*, 2020, **40**, 1602–1613.
5 G. Xu, X. Zhao, S. Zhao, C. Chen, M. J. Rogers, R. Ramaswamy and J. He, *Environ. Sci. Technol.*, 2021, **55**, 4205–4226.
6 K. Vorkamp and F. F. Rigét, *Chemosphere*, 2014, **111**, 379–395.
7 Y.-Z. She, J.-P. Wu, Y. Zhang, Y. Peng, L. Mo, X.-J. Luo and B.-X. Mai, *Environ. Pollut.*, 2013, **174**, 164–170.
8 C. A. Martínez-Huitle, M. A. Rodrigo and O. Scialdone, *Electrochemical water and wastewater treatment*, Butterworth-Heinemann, 2018.
9 E. T. Martin, C. M. McGuire, M. S. Mubarak and D. G. Peters, *Chem. Rev.*, 2016, **116**, 15198–15234.
10 P. Kar and B. Mishra, *J. Environ. Chem. Eng.*, 2016, **4**, 1962–1969.
11 C. K. da Silva-Rackov, W. A. Lawal, P. A. Nfodzo, M. M. Vianna, C. A. do Nascimento and H. Choi, *Appl. Catal., B*, 2016, **192**, 253–259.
12 A. Yazdanbakhsh, A. Eslami, G. Moussavi, M. Rafiee and A. Sheikhmohammadi, *Chemosphere*, 2018, **191**, 156–165.
13 C. Zhang, D. Zhang, Z. Li, T. Akatsuka, S. Yang, D. Suzuki and A. Katayama, *Environ. Sci. Technol.*, 2014, **48**, 6318–6325.
14 L. Yu, Y. Yuan, J. Tang, Y. Wang and S. Zhou, *Sci. Rep.*, 2015, **5**, 16221.
15 L. Wang, B. Batchelor, S. D. Pillai and V. S. Botlaguduru, *Chem. Eng. J.*, 2016, **302**, 58–68.
16 M. Trojanowicz, I. Bartosiewicz, A. Bojanowska-Czajka, K. Kulisa, T. Szreder, K. Bobrowski, H. Nichipor, J. F. Garcia-Reyes, G. Nałęcz-Jawecki and S. Męczyńska-Wielgosz, *Chem. Eng. J.*, 2019, **357**, 698–714.
17 R. Wang, T. Tang, G. Lu, K. Huang, H. Yin, Z. Lin, F. Wu and Z. Dang, *Environ. Pollut.*, 2018, **240**, 745–753.
18 B. Vanrenterghem, P. Jovanovič, M. Šala, M. Bele, V. S. Šelih, N. Hodnik and T. Breugelmans, *Electrochim. Acta*, 2018, **286**, 123–130.
19 S. Chen, W. Chu, H. Wei, H. Zhao, B. Xu, N. Gao and D. Yin, *Sep. Purif. Technol.*, 2018, **203**, 226–232.
20 Z. Lou, Y. Li, J. Zhou, K. Yang, Y. Liu, S. A. Baig and X. Xu, *J. Hazard. Mater.*, 2019, **362**, 148–159.
21 M. Yan, Z. Chen, N. Li, Y. Zhou, C. Zhang and G. Korshin, *Water Res.*, 2018, **136**, 104–111.
22 K. Zhu, X. Wang, X. Ma, Z. Sun and X. Hu, *Electrocatalysis*, 2019, **10**, 35–44.
23 J. Cheng, C. D. Vecitis, H. Park, B. T. Mader and M. R. Hoffmann, *Environ. Sci. Technol.*, 2010, **44**, 445–450.
24 R. Wang, T. Tang, J. Xie, X. Tao, K. Huang, M. Zou, H. Yin, Z. Dang and G. Lu, *J. Hazard. Mater.*, 2018, **354**, 1–7.
25 R. Qu, C. Li, J. Liu, R. Xiao, X. Pan, X. Zeng, Z. Wang and J. Wu, *Environ. Sci. Technol.*, 2018, **52**, 7220–7229.
26 L. Li, W. Chang, Y. Wang, H. Ji, C. Chen, W. Ma and J. Zhao, *Chem. – Eur. J.*, 2014, **20**, 11163–11170.
27 W. Guo, J. Zou, B. Guo, J. Xiong, C. Liu, Z. Xie and L. Wu, *Appl. Catal., B*, 2020, **277**, 119255.
28 Y. Lv, X. Cao, H. Jiang, W. Song, C. Chen and J. Zhao, *Appl. Catal., B*, 2016, **194**, 150–156.
29 S. M. Senaweera, A. Singh and J. D. Weaver, *J. Am. Chem. Soc.*, 2014, **136**, 3002–3005.
30 I. Ghosh, T. Ghosh, J. I. Bardagi and B. König, *Science*, 2014, **346**, 725–728.
31 C. Michelin and N. Hoffmann, *ACS Catal.*, 2018, **8**, 12046–12055.
32 J.-H. Shon and T. S. Teets, *ACS Energy Lett.*, 2019, **4**, 558–566.
33 A. Fujishima, X. Zhang and D. A. Tryk, *Surf. Sci. Rep.*, 2008, **63**, 515–582.
34 P. Xu, G. M. Zeng, D. L. Huang, C. L. Feng, S. Hu, M. H. Zhao, C. Lai, Z. Wei, C. Huang and G. X. Xie, *Sci. Total Environ.*, 2012, **424**, 1–10.
35 X. Wu, S. Xie, H. Zhang, Q. Zhang, B. F. Sels and Y. Wang, *Adv. Mater.*, 2021, **33**, 2007129.
36 K. Zhang and L. Guo, *Catal. Sci. Technol.*, 2013, **3**, 1672–1690.
37 T. Di, Q. Xu, W. Ho, H. Tang, Q. Xiang and J. Yu, *ChemCatChem*, 2019, **11**, 1394–1411.
38 H. Chen, H. S. Jena, X. Feng, K. Leus and P. Van Der Voort, *Angew. Chem., Int. Ed.*, 2022, **61**, e202204938.
39 Y. Zhang, F. Mao, L. Wang, H. Yuan, P. F. Liu and H. G. Yang, *Sol. RRL*, 2020, **4**, 1900438.
40 Q. Yang, M. Luo, K. Liu, H. Cao and H. Yan, *Appl. Catal., B*, 2020, **276**, 119174.
41 J. Qiu, X. Zhang, Y. Feng, X. Zhang, H. Wang and J. Yao, *Appl. Catal., B*, 2018, **231**, 317–342.
42 C. Han, S. Xiang, M. Ge, P. Xie, C. Zhang and J. X. Jiang, *Small*, 2022, **18**, 2202072.
43 J. Feng, J. Cheng, J. Pang, M. Tang, Z. Liu, C. Rong and R. Tan, *Catal. Sci. Technol.*, 2022, **12**, 6865–6874.
44 Q. Meng, H. Lv, M. Yuan, Z. Chen, Z. Chen and X. Wang, *ACS Omega*, 2017, **2**, 2728–2739.
45 N. Zhang, J.-J. Li, Y. Li, H. Wang, J.-Y. Zhang, Y. Liu, Y.-Z. Fang, Z. Liu and M. Zhou, *J. Colloid Interface Sci.*, 2022, **608**, 3192–3203.